Supporting Information

Biomimetic Self-Reinforcing Recyclable Biomass-Derived Sustainable Materials

Rui-Zhi Wu, Xing-Liang Li*, Huan-Sheng Cai, Ning Zhao, Xiu-Li Wang, Yu-Zhong Wang and Teng Fu*

Experimental Procedures

1.1 Raw materials

Dimethyl furan-2,5-dicarboxylate (DMFD, purity >99%) was purchased from ChemTarget Co., Ltd. (China). Sodium hydroxide (NaOH, purity ≥96%), and 1,4-Butanediol (1,4-BDO, purity ≥99.0%) were obtained from Aladdin Reagent (Shanghai) Co., Ltd. (China). Titanium (IV) n-butoxide (TBT, purity 99%) and Daidzein (DDF, purity ≥97%) were supplied by Adamas Co., Ltd. (China). Polylactide Diol, with an average molecular weight of approximately 1000 (PLA1000), was also sourced from Adamas Co., Ltd. (China). N, N-Dimethylformamide (DMF, purity 99.8%, Water ≤50 ppm by Karl Fischer) and 2-Ethyl-2-(Hydroxymethyl)-1,3-Propanediol (TMP, purity 99%) were purchased from Adamas Co., Ltd. (China). Ethylene carbonate (EC, purity ≥99% by GC), 1,4-Butanediol (BDO, purity ≥99.0%), and Isophorone diisocyanate (IPDI, purity ≥99.0%) were obtained from Aladdin Reagent (China). Hydrochloric acid (HCl) and ethanol (EtOH, purity 99%) were purchased from Kelong Chemical Factory

(Chengdu, China). N, N-Dimethylacetamide (DMAc, purity 98%) was also sourced from Kelong Chemical Factory (Chengdu, China). All other reagents were used as received without any further purification.

1.2 Synthesis of DDF-OH monomer

The synthesis of DDF-OH was performed as detailed in the accompanying Fig.S1. A 100 mL flask with three necks was filled with DDF (12.7 g, 0.05 mol), EC (17.6 g, 0.20 mol), KI (2 g), and DMAc (40 mL). Under a nitrogen atmosphere, the reaction mixture was heated to 130 °C for 12 hours. DDF-OH, a yellow solid product, was obtained by subjecting the mixture to alkali at the end of the reaction. The ^{1}H NMR and ^{13}C NMR spectra of the products are presented below, with the spectral data illustrated in Fig. S2. The ^{1}H NMR (DMSO-d6, δ, ppm) signals include: The peak between 8.42 and 7.00 ppm is attributed to the protons on the benzene ring and conjugated system. The peaks at 4.88 and 4.96 ppm are assigned to the protons on the hydroxyl group. The peaks in the range of 4.15 to 3.73 ppm are attributed to the protons on the methylene groups. In the 13C NMR (DMSO-d6, δ, ppm) spectrum, the peak between 163.37 and 101.25 ppm is attributed to the carbons in the benzene ring and conjugated system. The peaks at 69.77 and 59.54 ppm are assigned to the carbons in the methylene groups.

1.3 Synthesis of PAOM

The PAOM polyesters were synthesized via a two-step process involving transesterification and polycondensation. Four copolyesters (PAOM-1, PAOM-2, PAOM-3, and PAOM-4) with different DMFD/DDF-OH molar ratios (100/2.5, 100/5, 100/7.5, and 100/10) were synthesized in this work. Taking the synthesis of PAOM-4 as an example, DMFD (36.8 g, 0.20 mol), BDO (36.0 g, 0.40 mol), DDF-OH (6.84 g, 0.02 mol), and TBT (0.01 g as a catalyst) were added to a 100 mL three-necked flask equipped with a stirrer, water separator, and N_2 inlet pipe. The transesterification was conducted at 185 °C for 4 hours. Subsequently, the polycondensation was carried out at 235 °C under a vacuum of 80–125 Pa for 3 hours.

In the ^{1}H NMR spectra (Fig. S2a, Fig. S3-S6), the chemical shift at 7.33 ppm is attributed to the H_b protons in the furan ring. The peak at 8.70 ppm corresponds to the H_a protons on the double bond. The peaks at 8.41, 7.48, 7.39, 7.14, and 7.12 ppm are assigned to the aromatic protons in the benzene ring, while the peaks at 4.91 and 4.84 ppm correspond to the methylene protons in the DDF-OH unit. Additionally, the peaks at 4.51 and 1.98 ppm are associated with the protons in the BDO unit. As the DDF-OH content increases, the intensity of Ha gradually increases, while the H_a in the DMFD unit decreases. The experimental content of the DDF-OH and DMFD units was calculated by the integration ratio of H_a to H_b, which was consistent with the feed ratio (Table S2). The characteristic absorption peaks of the furan ring were observed in the ATR-FTIR spectra (Figures S2a, S2b). The peak at 1711 cm^{-1} is attributed to the

stretching vibration of the C=O bond in the furan ring ($\nu_{C=O}$), while the peak at 1124 cm^{-1} is due to the in-plane deformation vibration of the C-O bond (ν_{C-O}).

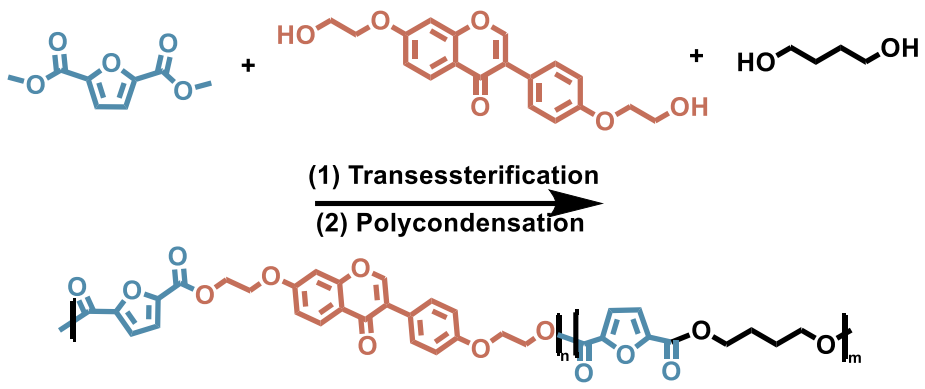

Scheme S1. Schematic diagram of PAOM.

1.4 Chemical recycling experiments

Under mild solvent conditions, PAOM-4 can undergo quantitative chemical recycling. A mixture of PAOM-4 (10.0 g), NaOH (10 g), ethanol (25 g), water (50 g), and BDO (25 g) was placed in a 150 mL flask and reacted in an oil bath at 90°C for 4 hours, leading to the spontaneous separation of sodium furan-2,5-dicarboxylate and the DDF-OH monomer from the solution. The sodium furan-2,5-dicarboxylate, DDF-OH monomer, and filtrate were collected by filtration. Subsequently, the sodium furan-2,5-dicarboxylate was dissolved in 100 mL of water, and the DDF-OH monomer was separated again by filtration. After cooling, concentrated hydrochloric acid (>99%) was added to adjust the pH of the solution to 2. At this point, the sodium furan-2,5-

dicarboxylate was converted into recovered rFDCA, which was then isolated by filtration (Scheme S2).

In the ^{1}H NMR spectrum (Fig. 6C), the chemical shift at 13.6 ppm is attributed to H_a in the carboxyl group, while the chemical shift at 7.3 ppm is assigned to H_b in the furan ring. The signals of the carboxyl group and the furan ring (C_a, C_b and C_c) in the ^{13}C NMR spectrum appear at 159.4, 147.5, and 118.9 ppm, respectively (Fig. S20-21). The purity of rFDCA, as determined by liquid chromatography, exceeds 99.0% (Fig. 6D).

The ^{1}H NMR, ^{13}C NMR, and LC data of rBDO are presented as follows (S24–S26). In the ^{1}H NMR spectrum (D_2O, δ, ppm), the peak at 4.7 ppm is attributed to the hydroxyl group proton H_a. The peaks at 3.55 ppm and 1.52 ppm correspond to the methyl group protons H_b and H_c, respectively. ^{13}C NMR spectrum (D_2O, δ, ppm), the peak at 61.2 ppm and 29.6 ppm are assigned to the C_a and C_b on the methyl group. The LC data indicate that the purity of rBDO is 99.8%.

1.4.2 Schematic diagram of recycling of PAOM polyester.

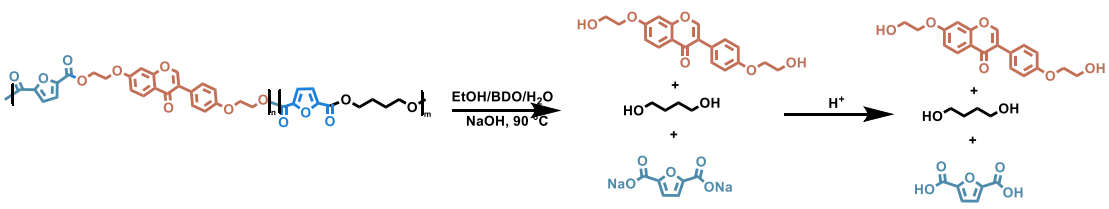

Scheme S2. Schematic diagram of recycling of PAOM polyester.

1.4.3 Synthesis of rDMFD by rFDCA.

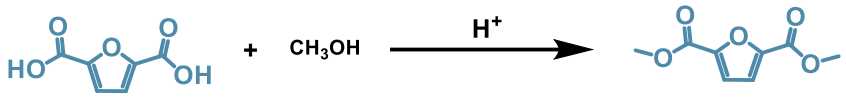

Scheme S3. Schematic synthesis of rDMFD.

1.4.4 Synthesis of rDMFD and repolymerization of rPAOM-4.

rDMFD was synthesized from rFDCA (**Scheme S3**). A mixture of 36 g of rFDCA, 1 mL of sulfuric acid, and 160 mL of methanol was added to a 500 mL three-necked flask and reacted at 90 °C for 6 hours. After the reaction, the precipitate was collected by filtration and washed three times with distilled water to obtain rDMFD. The obtained rDMFD was then used for the repolymerization of recovered PAOM-4 (rPAOM-4). The synthetic route for rPAOM-4 is the same as that for PAOM-4.

The 1H NMR, ^{13}C NMR, and LC data of rDMFD are presented as follows (Fig. 6E, S16–S18). In the ^{1}H NMR spectrum (DMSO-d6, δ, ppm), the peak at 7.44 ppm is attributed to the H_a proton on the furan ring, while the peak at 3.87 ppm is assigned to the H_b proton on the methyl group. In the ^{13}C NMR spectrum (DMSO-d6, δ, ppm), the peak at 52.9 ppm corresponds to the C_a carbon on the methyl group. The peaks at 119.5 ppm and 146.5 ppm are attributed to the C_b and C_c carbons on the furan ring, respectively. The peak at 158.3 ppm corresponds to the C_d carbon in the carbonyl group. The LC data indicate that the purity of rDMFD is greater than 99.0% (Fig.6F).

1.4.5 Synthesis of up-PU.

The synthesis route of up-PU is shown in Scheme 4. 10.0 g of PLA1000 was added to a 150 mL round-bottom flask and vacuum-dehydrated at 120 °C for 1 hour. Then, 0.36 g of rDFCA, 0.85 g of rDDF-OH, 5.32 g of IPDI, 0.01 g of DBTDL, and 20 mL of DMF were added and reacted at 80 °C for 4 hours. Afterward, 0.89 g of TMP was added, and the mixture was stirred for 3 minutes. The reaction solution was then poured into a PTFE container and cured in a vacuum oven at 80°C for 24 hours. After removing the solvent, up-PU was obtained.

In the FTIR spectra (Fig. 6K), the stretching vibration peak of the methylene (-CH_2-) groups in the molecular chain appears at 2840 cm^{-1}. The strong absorption peak at 1098 cm^{-1} corresponds to the ether bond (C-O-C) in PTMG. The absence of a peak at 2260 cm^{-1} indicates the complete reaction of the -NCO groups in IPDI. The characteristic absorption peak of the urethane carbonyl (C=O) group is observed at 1700 cm^{-1}.

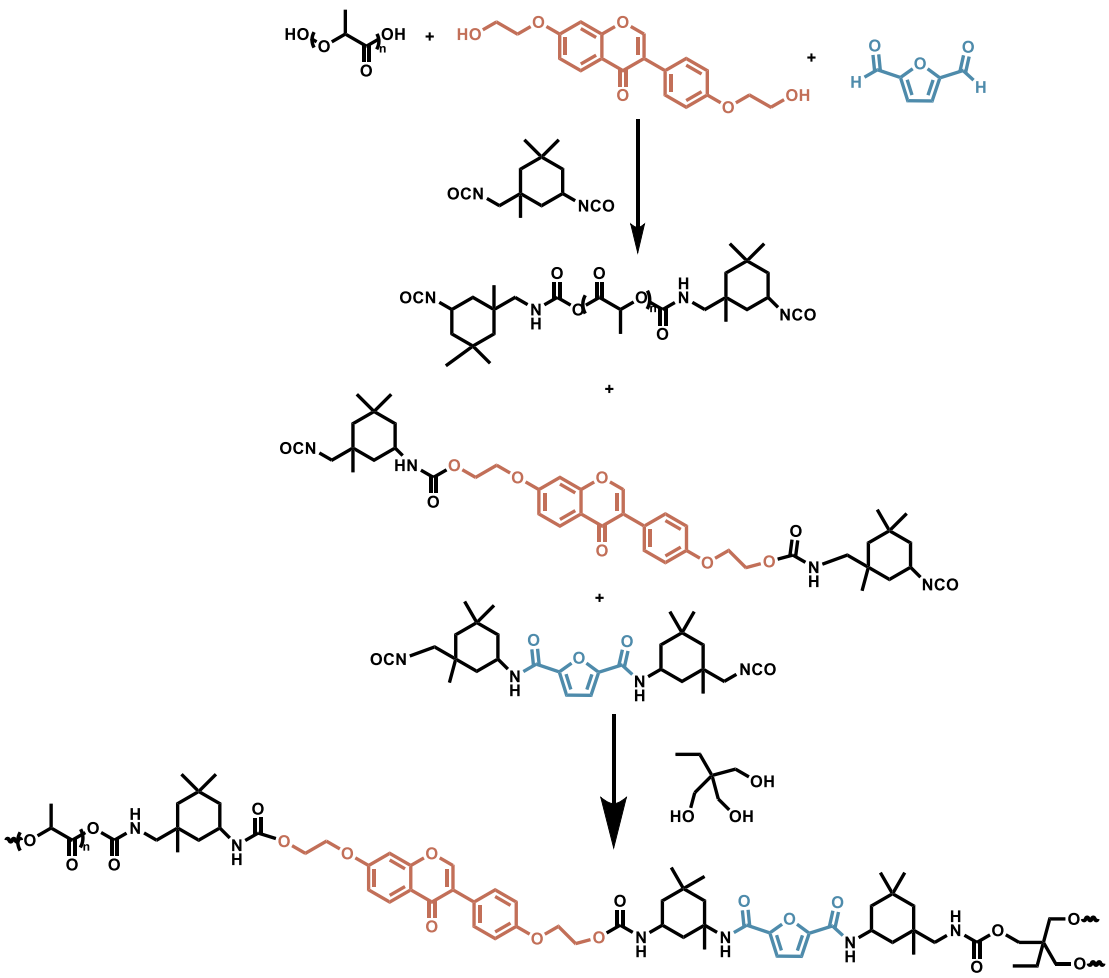

Scheme S4. Schematic synthesis of up-PU.

1.5 Characterization

The chemical structure of the PAOM, rFDCA, rDMFD and rBDO were characterized using ^{1}H NMR and ^{13}C NMR spectroscopy. The ^{1}H NMR and ^{13}C NMR spectra were recorded on a Bruker AC-P 400 MHz NMR instrument and a MesoMR23-060H-I instrument (Shanghai, China). Deuterated trifluoroacetic acid (TFA) was used as the solvent for the copolyesters, while DMSO-d6 and D_2O were used for the monomers.

Low-field nuclear magnetic resonance (LF-NMR) spectra were recorded using a VTMR20-010V-I in situ variable temperature NMR analyzer.

The FT-IR spectra were obtained using a Nicolet 6700 spectrometer. The intrinsic viscosity [η] of the PAOM was determined using an Ubbelohde viscometer. All samples were dissolved in a 50/50 (v/v) phenol/1,1,2,2-tetrachloroethane solution at 25 °C. The intrinsic viscosity of the polyesters was calculated according to Equation (1).

$$[\eta]=\frac{[2\{t/t_0\text{-}\ln(t/t_0)\text{-}1\}]^{\frac{1}{2}}}{c} \quad (1)$$

c is the solution concentration, t is the flow time of the solution, and t_0 is the flow time of the solvent. The reported values are the average of three measurements.

The Restrained Electrostatic Potential (RSEP) charges for all molecules were fitted using the Multiwfn software, and the top file was obtained using the Sobtop software [1,2]. The initial molecular simulation files were generated using Packmol software [3], with the number of molecules set according to the specified ratios. Molecular dynamics simulations were performed using Gromacs 5.03 software [4], employing the OPLS-AA (Optimized Potentials for Liquid Simulations All-Atom) force field [5]. Energy minimization was first carried out, followed by NPT ensemble simulation at 300 K using the Berendsen pressure coupling method to achieve system equilibration. The time step was set to dt = 2 fs, with a total simulation time of 2 ns, and outputs were recorded every 1 ps. The Parrinello-Rahman pressure coupling method was then applied for an additional 2 ns NPT simulation. The temperature was then ramped up to

450 K for a 5 ns NPT simulation, and after that, a 10 ns NPT simulation was performed at 300 K to achieve system equilibrium. Finally, the v-rescale temperature coupling method was used for a 20 ns NVT ensemble simulation for production analysis, with all the figures obtained using VMD software [6].

Dynamic rheological tests were conducted using a Discovery HR-30 rheometer equipped with a 25 mm diameter parallel-plate geometry. Dynamic oscillatory shear measurements were performed across a frequency range of 0.01 to 100 Hz at 190 °C, under a strain of 1%, with a gap size of 1000 μm.

Differential scanning calorimetry (DSC) curves were acquired using a NETZSCH DSC 214 instrument. 5 mg of each sample was placed in alumina crucibles and scanned from 10 to 270 °C at a heating rate of 5 °C/min.

Thermogravimetric analysis (TGA) was performed using a NETZSCH TG 209 F1 thermogravimetric analyzer in a nitrogen atmosphere. Samples weighing 3-5 mg were heated from 40 °C to 700 °C at a rate of 10 °C/min.

The crystallinity of the copolyesters was characterized using wide-angle X-ray scattering (WAXS) on a Panalytical X'Pert MPD Pro diffractometer. The instrument utilized copper Kα1 radiation (λ = 1.5406 Å) and was equipped with an X'Celerator detector. The samples were scanned over a 2 θ angle range of 5° to 45°.

Positron annihilation lifetime spectroscopy (PALS) tests were conducted using a Finder1000 PALS system (model PLS-System). The positron source had a time resolution of 0.23 ns, and two small discs measuring 25 mm × 25 mm × 1 mm were placed between the ^{22}Na positron source. The positron lifetime was determined by

measuring the time delay between the emission of one of the birth gammas (1.28 MeV) and the detection of the resulting 0.511 MeV annihilation photons.

The breakdown field strength of polyesters and copolyesters was assessed using a DDJ-50KV instrument, with the applied voltage ramped at a rate of 1 kV/s. The surface resistivity of the copolyesters was measured using an ST2742B instrument.

The micro combustion calorimetry (MCC) of the materials was evaluated using an FAA-PCFC instrument.

The mechanical properties of the copolyesters were evaluated using an Instron Universal Testing Machine (model 5567) at a crosshead speed of 5 mm/min at room temperature. Three specimens were tested for each sample, and the average result was reported.

The barrier properties to O_2 and CO_2 were analyzed using a manometric method with a Labthink VAC-V2 permeance testing device. The polyesters were prepared as circular discs with a thickness of 0.5 mm and a diameter of 50 mm. The gas permeability coefficient was recorded continuously until a stable permeability rate was achieved.

The UV-shielding properties of the copolyesters were evaluated using a Cary Eclipse spectrometer (Agilent, USA) at room temperature, across a wavelength range of 200–800 nm.

The hygrothermal aging test was conducted by placing the copolyester in a constant temperature and humidity chamber (ZH-TH-800) at 60 °C and 99% relative humidity for 100 hours, followed by testing its mechanical properties.

The water absorption test was performed by placing the copolyester in a constant temperature and humidity chamber (ZH-TH-800) at room temperature (25 °C) and 99% relative humidity for 24 hours, and then measuring the change in mass.

Space charge testing was conducted using a Japan-made Fivelab Peanuts instrument, with polarization for 30 minutes followed by depolarization for 30 minutes.

The purity of rFDCA, rDMFD, and rBDO was determined using liquid chromatography (LC) with a Finnigan TSQ Quantum mass spectrometer. The recycled liquid was analyzed using gas chromatography (GC) with an Agilent 7890B instrument, employing methanol as the solvent.

The solvent resistance of the copolyester films was assessed by immersing the samples in various solvents, including deionized water (H_2O), ethanol (EtOH), acetone (ACE), dimethyl sulfoxide (DMSO), methanol (MeOH), 5 wt% aqueous sodium hydroxide (NaOH), N, N-dimethylformamide (DMF), and tetrahydrofuran (THF), for 7 days at room temperature and pressure. The physical and chemical changes in the samples were then compared before and after exposure to these solvents.

Results and Discussion

Structural Characterizatio

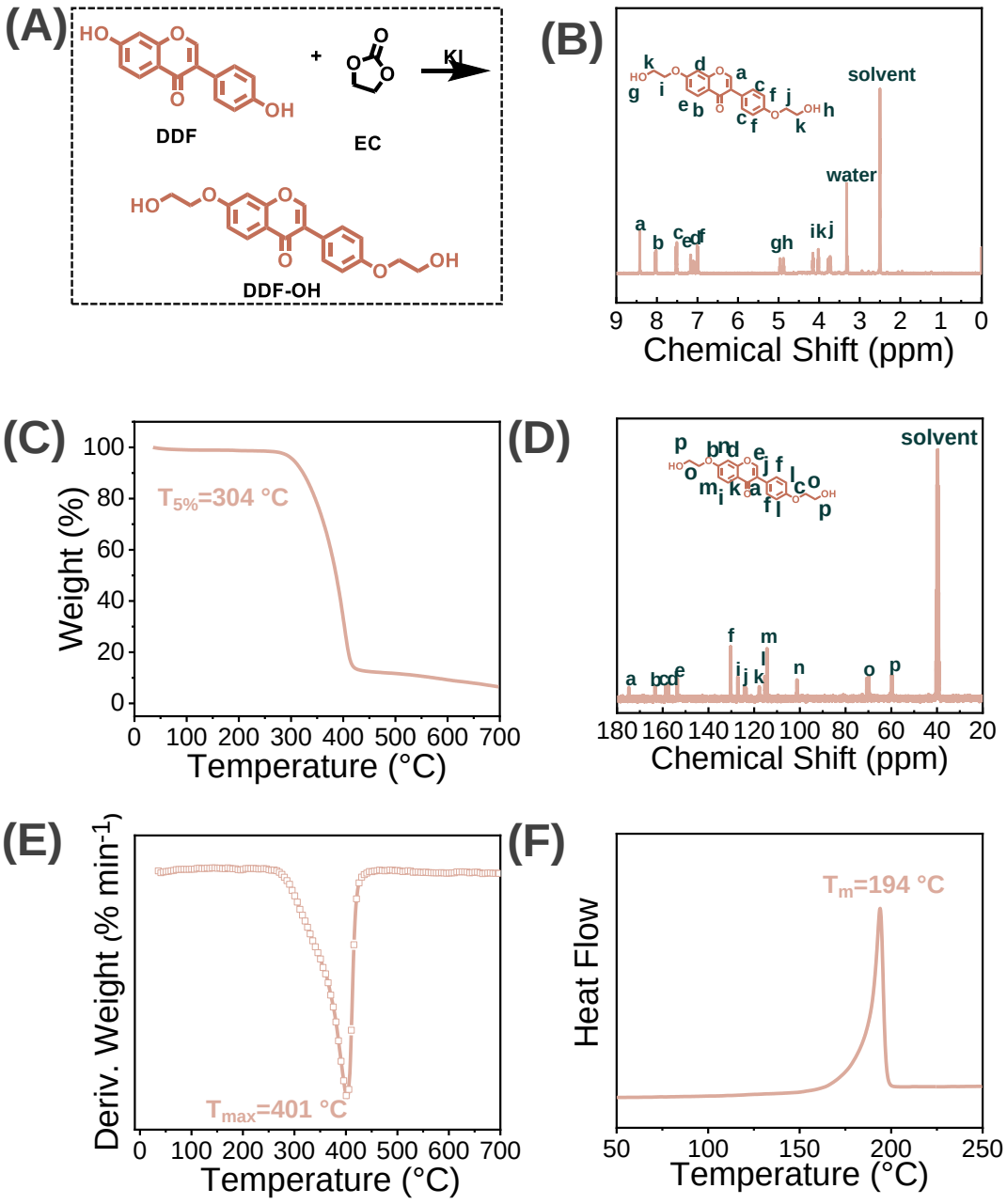

Figure S1. (A) Schematic synthesis of DDF-OH. (B) ^{1}H NMR spectra, (C) ^{13}C NMR spectra, (D–E) TGA curves, and (F) DSC curves of DDF-OH.

224 **Table S1.** Thermal properties of DDF-OH.

Samples	$T_{5\%}$ (°C)	T_{max} (°C)	T_b (°C)
DDF-OH	304	401	194

225

226

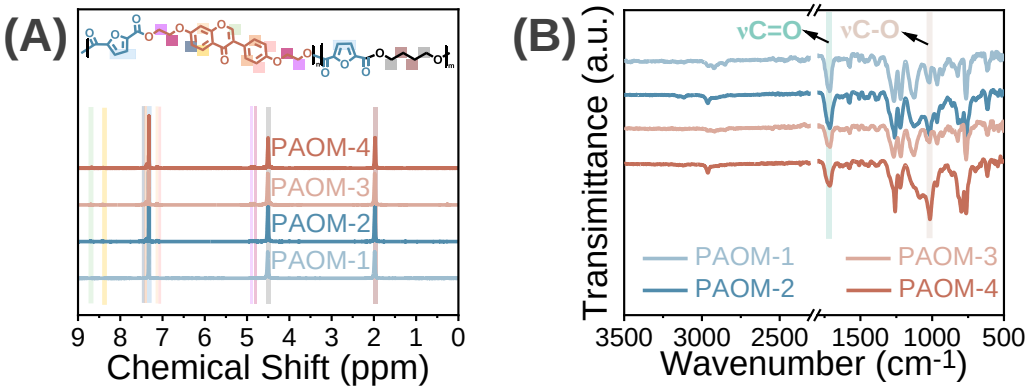

227

228 **Figure S2.** (A) ^{1}H NMR and (B) ATR-FTIR spectra of PAOM.

229

Table S2. Molar composition, intrinsic viscosity of PAOM.

Samples	$n_{DDF\text{-}OH}/n_{DMFD}$[a]	$n_{DDF\text{-}OH}/n_{DMFD}$[b]	$[\eta]$ (dL/g)
PAOM-1	2.5	2.4	1.1
PAOM-2	5	4.9	1.0
PAOM-3	7.5	7.4	1.0
PAOM-4	10	9.8	1.0

[a]The molar ratio of DDF-OH/DMFD feed. [b] Actual molar ratio of DDF-OH/DMFD in the PAOM.

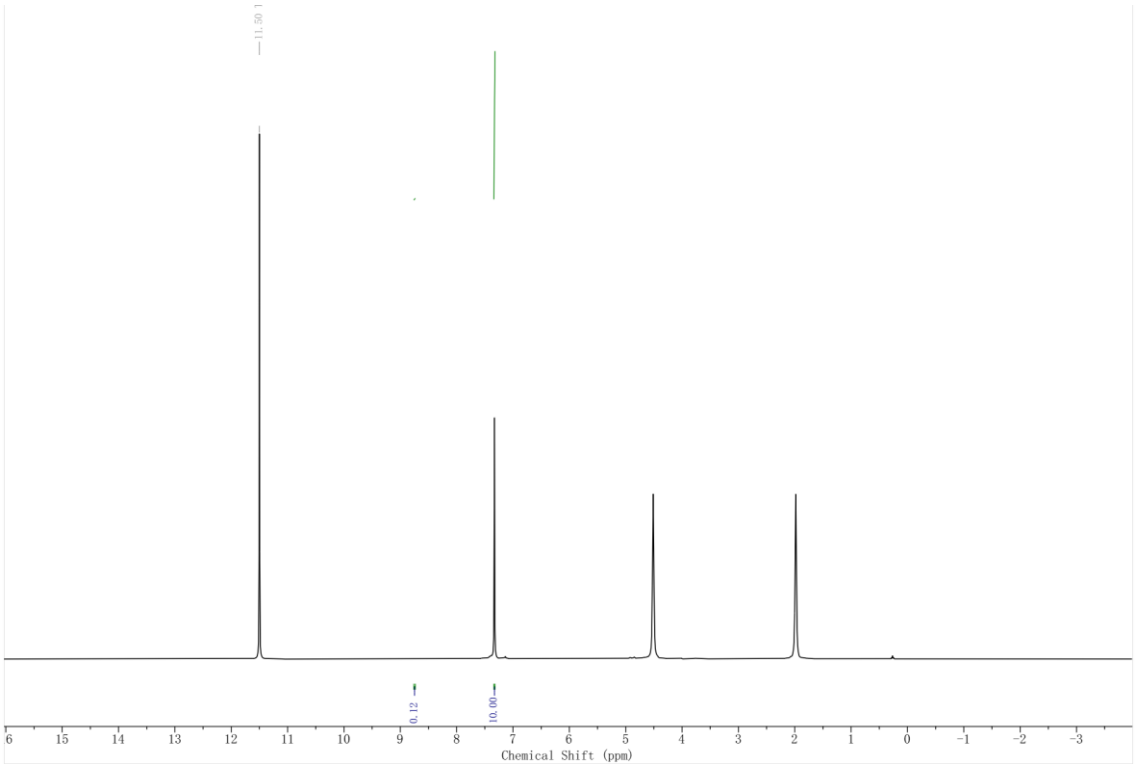

234

235 **Figure S3.** ^{1}H NMR spectra of PAOM-1.

236

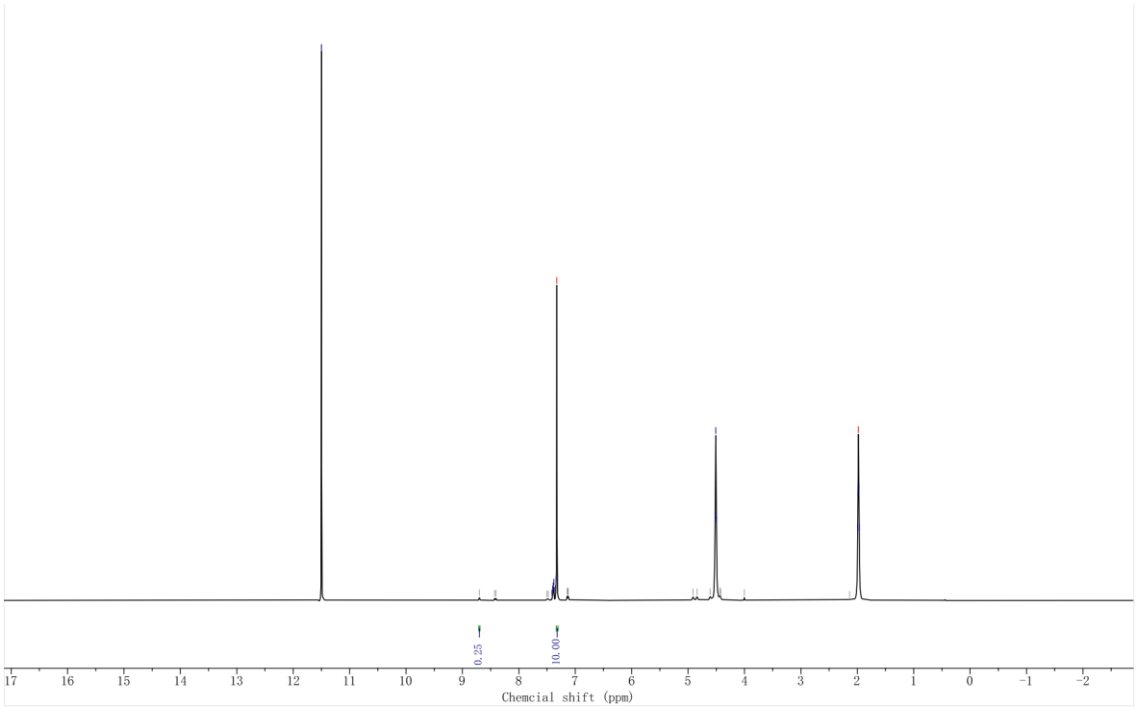

Figure S4. ^{1}H NMR spectra of PAOM-2.

240 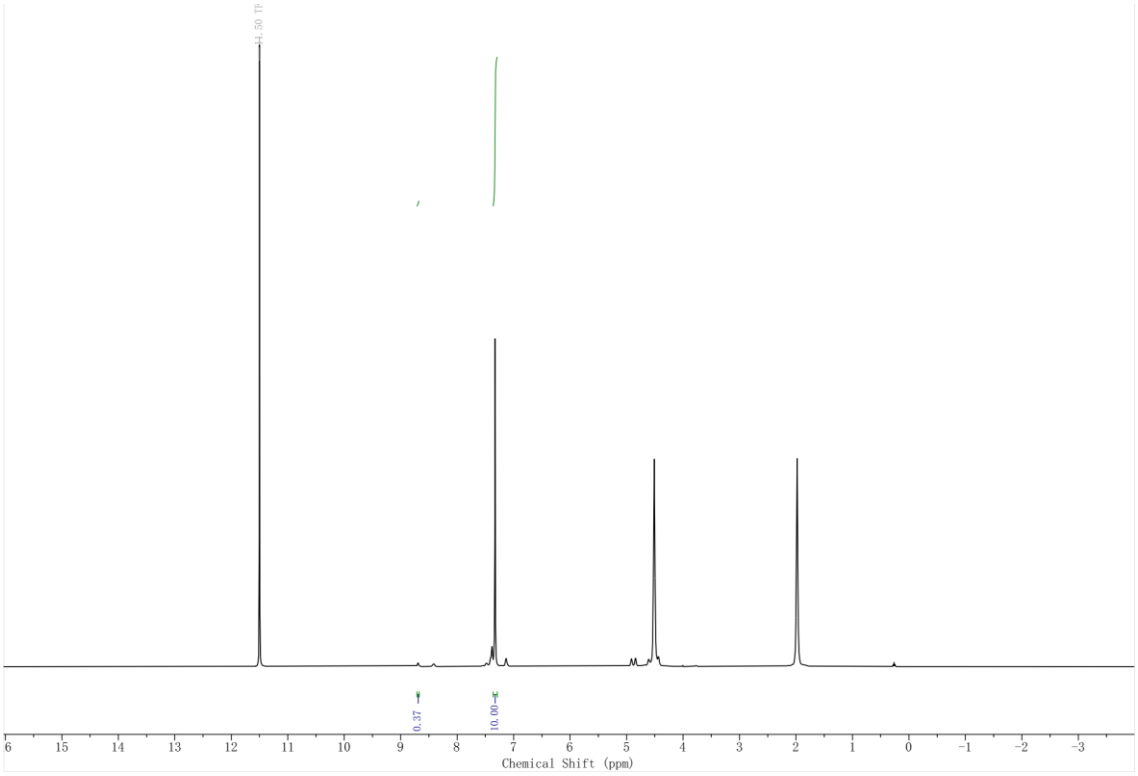

241 **Figure S5.** ^{1}H NMR spectra of PAOM-3.

242

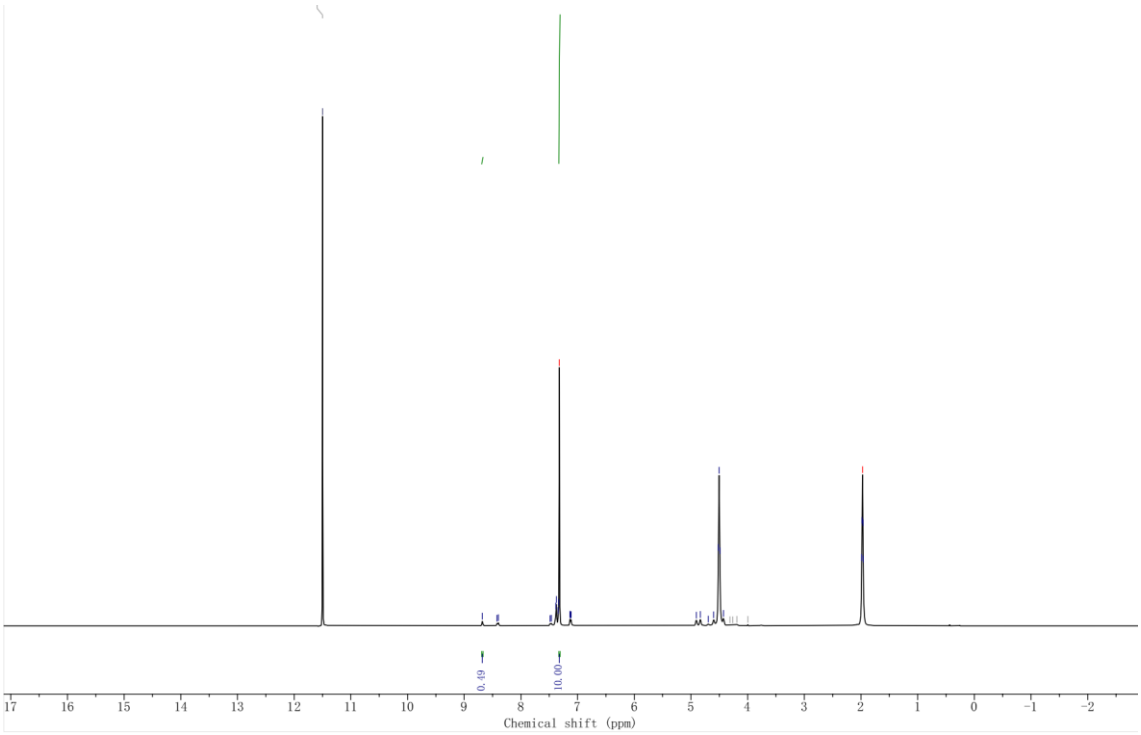

243

244 **Figure S6.** ^{1}H NMR spectra of PAOM-4.

245

Thermal and Crystallization Properties

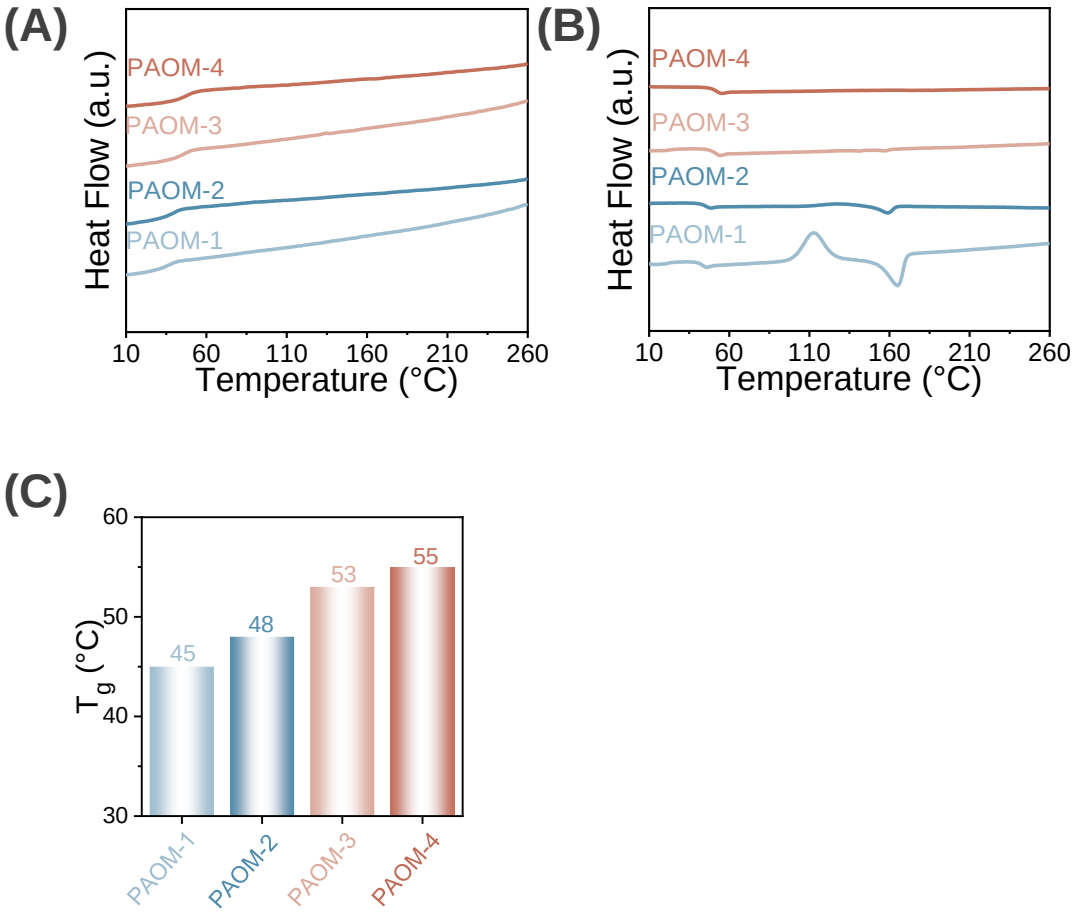

Figure S7. (A) DSC cooling and (B) 2nd heating scans of PAOM, (C) T_g testing plots.

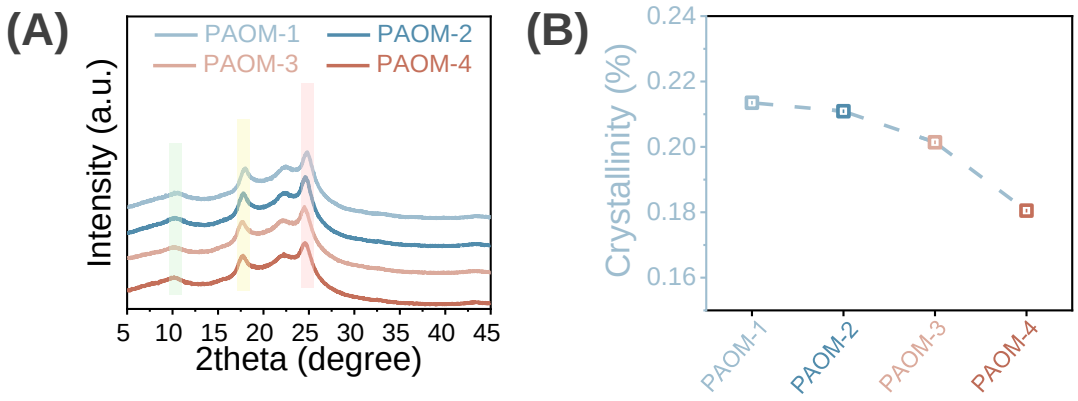

250

251 **Figure S8.** (A) XRD curves of thermal annealing PAOM, (B) X_c testing plots.

252

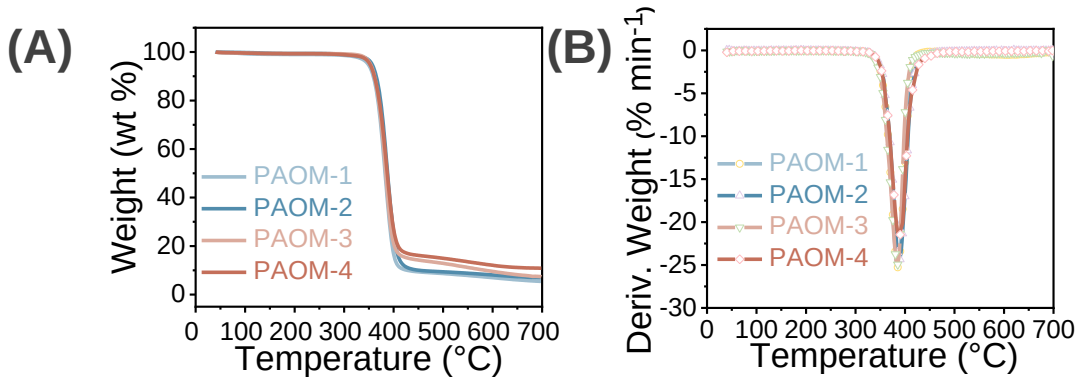

253

254 **Figure S9.** (A-B) TGA curves of PAOM.

255

Table S3. Thermal properties and degree of crystallinity for PAOM.

Samples	T_m (°C)	T_g (°C)	T_c (°C)	$T_{5\%}$ (°C)	T_{max} (°C)	*R700*	X_c[b] (%)
PAOM-1	165	45	113	348	385	5.5	21.4
PAOM-2	159	48		356	389	7.0	21.1
PAOM-3		53	-	354	385	7.4	20.1
PAOM-4		55	-	355	388	10.9	18.1

[a] Tested by the melting point apparatus. [b] Crystallinity degree (X_c) calculated by the deconvolution of amorphous and crystalline peaks in XRD patterns using the Origin.

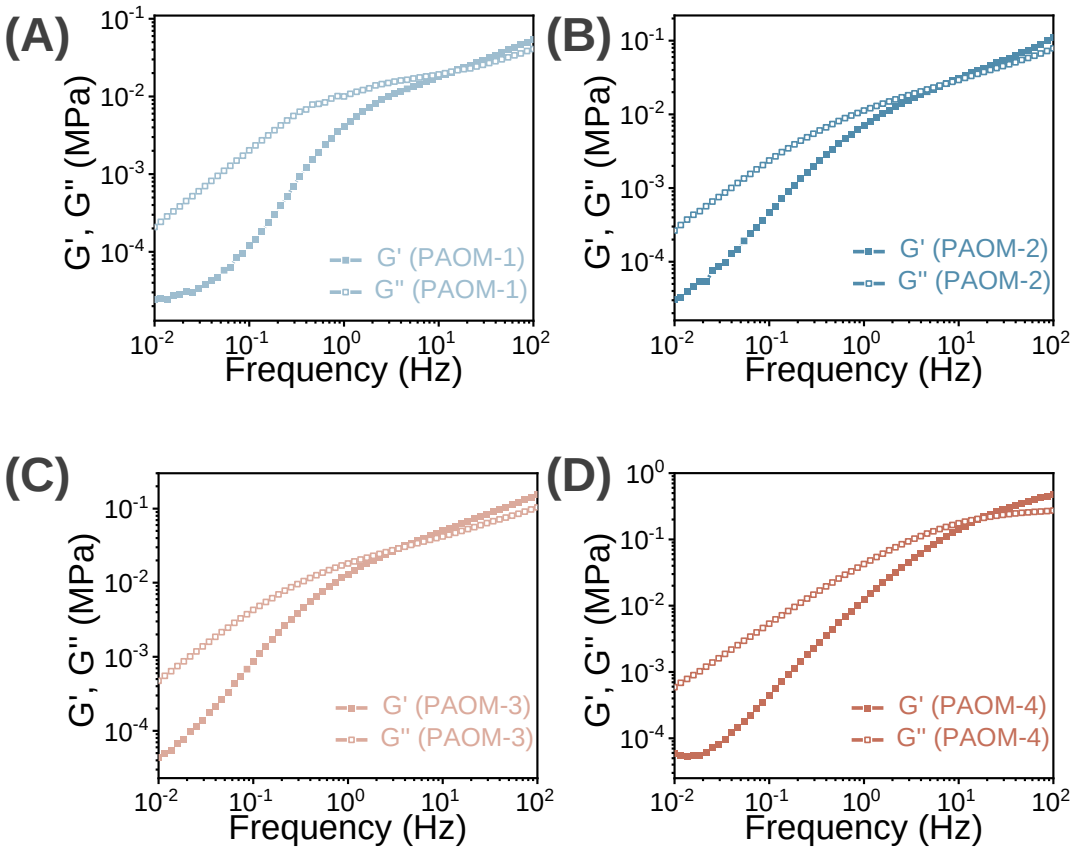

261

262 **Figure S10.** (A-D) Storage modulus (G') and loss modulus (G'') versus frequency of

263 PAOM.

264

Table S4. Zero-shear viscosity for PAOM.

Samples	η_0 (Pa s)
PAOM-1	3744.3
PAOM-2	4236.1
PAOM-3	7551.6
PAOM-4	9425.4

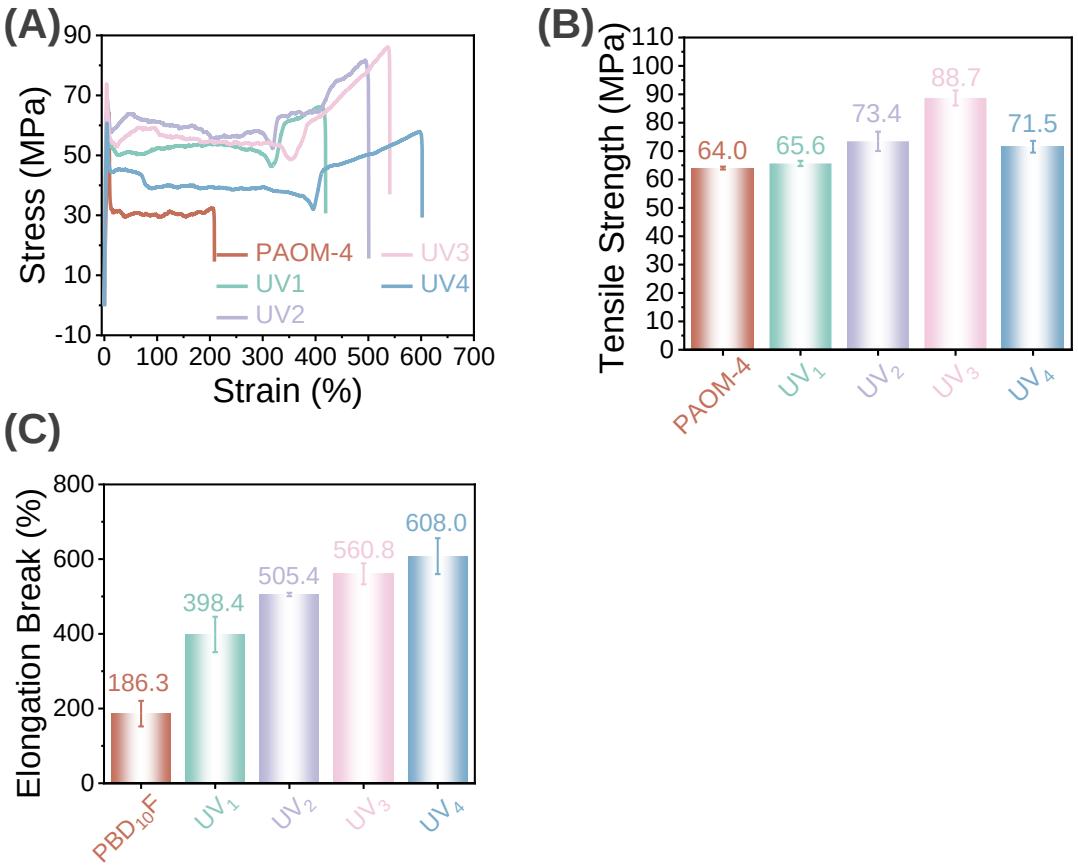

Figure S11. (A-C) Changes in the Mechanical Properties of PAOM Under Different UV Irradiation Times. The bar represents the mean value for three individual experiments, and the error bar is s.d. based on three individual experiments.

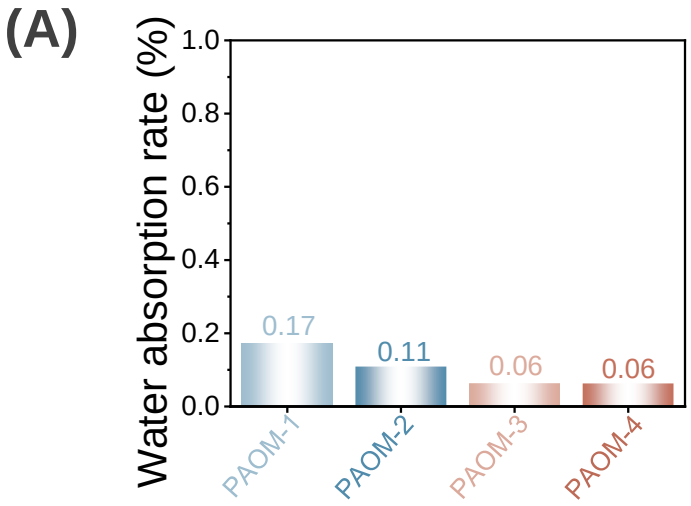

273

274 **Figure S12.** (A) Water absorption rate of PAOM.

275

Positron Annihilation Lifetime Spectrum (PALS)

The voids or pores of polymer materials can be detected by PALS, which utilizes positronium. (Usually, there are two types of positrons in polymer materials, namely the pair state (*p*-Ps, singlet spin state) and the ortho state (*o*-Ps, triplet spin state)). When positrons from a radioactive β-decay source stop in a porous material, the Ps is naturally formed by electron capture. Among them, *p*-Ps undergoe self-annihilation decay by emitting two kinds of gamma rays, with a lifetime of 125 ps. The self-annihilation lifetime of the three gamma rays emitted by *o*-Ps is 142 ns. Moreover, the positron in Ps will annihilate with either its bound electron or with electrons in the material surrounding the pore, which is highly sensitive to the size of the free volume. When annihilation occurs, the test will generate data for three exponential decay components (Lifetime 1 τ_1, Lifetime 2 τ_2, and Lifetime 3 τ_3), where τ_1 is due to the *p*-Ps lifetime and free annihilation lifetime of positrons. The component τ_2 is attributed to the annihilation of positrons in the amorphous region. τ_3 can be used to calculate the free volume of amorphous materials, which is attributed to the "pick-off" annihilation of *o*-Ps at the pores in the amorphous phase.

The radius *R* of the free volume can be calculated by Equation (Eq) S2.[7]

$$\tau_3=\frac{1}{2}\left[1-\frac{R}{R+\Delta R}+\frac{1}{2\pi}\sin\left(\frac{2\pi R}{R+\Delta R}\right)\right] \quad (2)$$

ΔR is the thickness of the electron layer in Eq S1, and its value is 0.166 nm.[8] As demonstrated in Table S1, the *o*-Ps intensity (I_3) of the PAOM decreased in decreasing

order as the DDF-OH content increased, implying that the number of free volume cavities decreased accordingly. Equation S3 expresses the free volume (F_V) of the PAOM, which is proportional to the size and number of cavities.

$$F_V = C\frac{4\pi}{3}R^3 I_3 \quad (3)$$

In Eq S2, C is the scaling factor for the spherical hole, which has a value of 1.5.[9]

Table S5. Summary of Ps lifetime components and corresponding pore sizes of PAOM.

Samples	τ_3 (ns)	I_3 (%)	R (Å)	F_v (%)
PAOM-1	1.6194	10.4867	0.2471	0.9935
PAOM-2	1.6421	9.9899	0.2495	0.9747
PAOM-3	1.6173	9.9188	0.2469	0.9371
PAOM-4	1.6027	9.6562	0.2453	0.8948

Mechanical Properties

Table S6. Mechanical properties of PAOM and many biomass-based and engineering plastics.

Samples	Tensile strength (MPa)	Elongation break (%)
PA[10]	85.3	25.5
PC[11]	68.5	9.8
POM[12]	68.7	40.2
PET[13]	55.5	100.3
PPO[14]	60.1	30.5
PTFE[15]	25.4	300.8
PEEK[16]	95.6	40.3
ABS[17]	45.2	20.5
PPS[18]	63.0	1.8
PI[19]	92	9.3
PBAT[20]	21.4	400
PLA[21]	58.4	7.0
PBF[22]	55.3	374.2
PHB[23]	31.6±1.8	228.0±24.6

Table S7. Gas permeability coefficients for PAOM and many biomass-based and engineering plastics.

Sample[a]	CO_2 (barrer) [a]	BIF p	O_2 (barrer) [b]	BIF p	H_2O (g/(m^2•24 h))	H_2O (g•cm/(cm^2•s•Pa))	BIF p
PE[24]	6.29	1.0	1.58	1.0	7.90	-	1.0
PET[25]	0.010	63.5	0.06	26.3	4.3	-	1.8
PP[26]	3.82	1.6	2.75	0.6	2.2	-	3.6
PEF[27]	0.04	161.2	0.02	105.3	-	1.64E-14	4.9
PBAT[28]	5.90	1.1	0.76	2.1		3.52E-13	0.2
PLA[28]	1.00	6.3	0.25	6.3		1.10E-13	0.7
PBF[22]	0.0385	163.4	0.0210	75.2	4.4509	4.488E-14	1.8
PAOM-1	1.81E-5	8.7E4	2.46E-5	2.6E5	1.0861	1.506E-14	7.3
PAOM-2	1.64E-5	9.6E4	2.31E-5	2.7E5	0.5430	9.105E-15	14.55
PAOM-3	1.61E-5	9.8E4	1.46E-5	4.3E5	0.5430	8.505E-15	14.55
PAOM-4	1.12E-5	1.4E5	1.30E-5	4.8E5	0.2715	3.852E-15	29.10

315 [a] The test was performed at 0.1 MPa. [b] CO_2 permeability coefficient, at 23 °C, 50%

316 relative humidity 1 barrer = 10^{-10} cm^3cm/cm^2•s•cm Hg, O_2 permeability coefficient, at

317 23 ℃, 50% relative humidity.

318

Conversion of UV Irradiation Time

The equivalent time calculation between 108 h UV irradiation and the natural environment.

The UV-A irradiation in the Ultra Concentrated UV Curing Lamp is about 3000 mW cm^{-2}. An effective irradiation of 0.2 W m^{-2} corresponds to a UV Index of 8. As shown in Equation S4, the UV irradiation in the UV light Ultra Concentrated UV Curing Lamp is equivalent to 150,000 times that in a natural environment with a UV index of 8. The annual average UV index in Chengdu, China, is 7~9.

$$3000\ \frac{\mathrm{mW}}{\mathrm{cm}^2}=30000\frac{\mathrm{W}}{\mathrm{m}^2}=150{,}000\times0.2\frac{\mathrm{W}}{\mathrm{m}^2} \quad (4)$$

The PAOM were exposed in Ultra Concentrated UV Curing Lamp for 3 h, which is almost equivalent to 450,000 h in a region with a UV index of 8. As shown in Equation S5.

$$30000\frac{\mathrm{W}}{\mathrm{m}^2}\times3\ \mathrm{h}=0.2\frac{\mathrm{W}}{\mathrm{m}^2}\times t \quad (5)$$

$$t=450{,}000\ \mathrm{h}\approx51\ \mathrm{years}$$

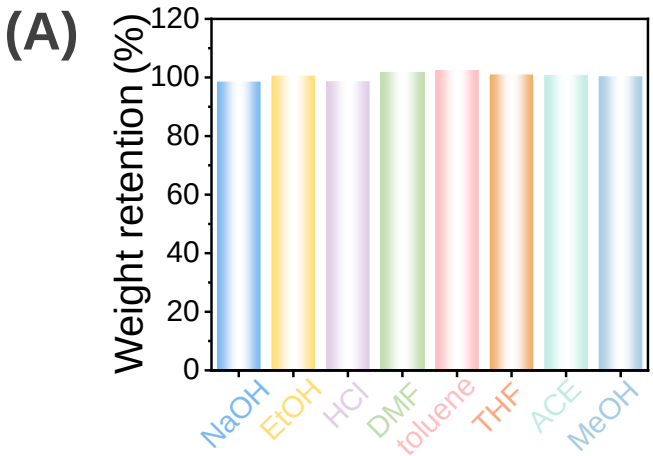

Figure S13. (A) Weight retention of PAOM films.

Table S8. Summary of the Weight retention (%) of PAOM-4 films after being soaked in different solvents for 7 days.

Samples	NaOH	EtOH	HCl	DMF	Toluene	THF	ACE	MeOH
Weight retention (%)	98.6	100.1	98.7	101.6	102.5	101.0	100.9	100.4

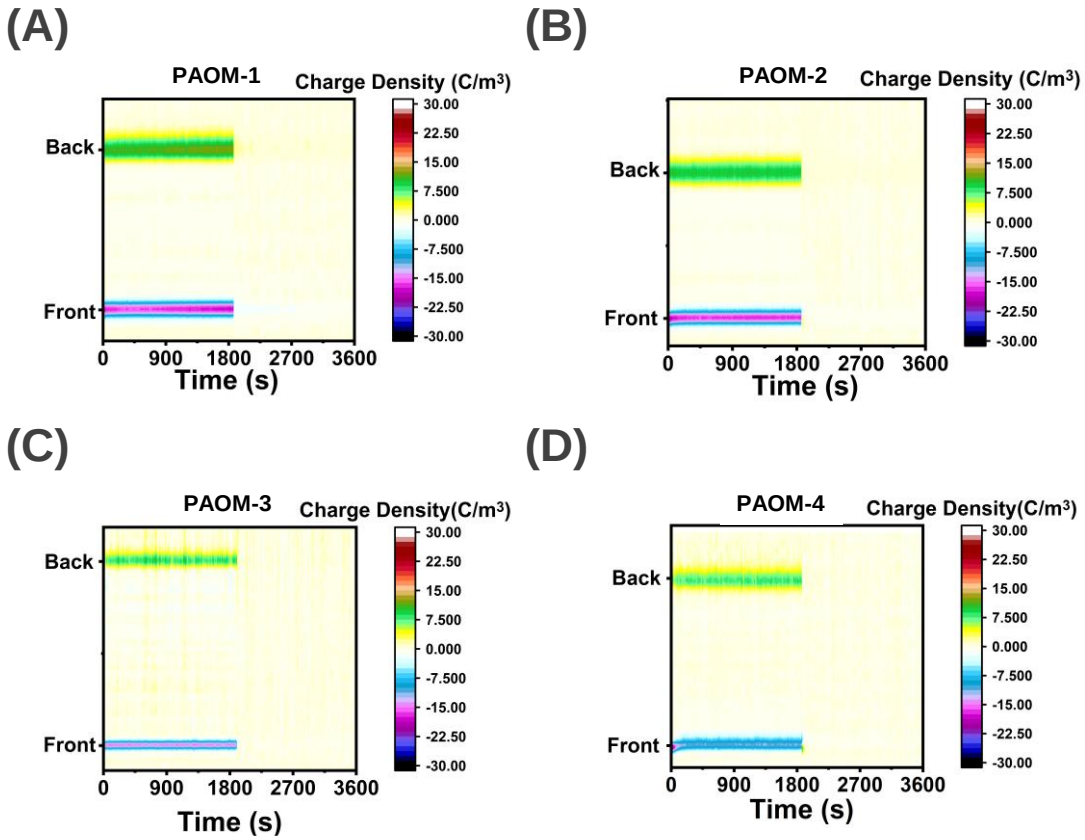

343

344 **Figure S14.** (A-D) Space charge distribution during space charge test of PAOM.

345

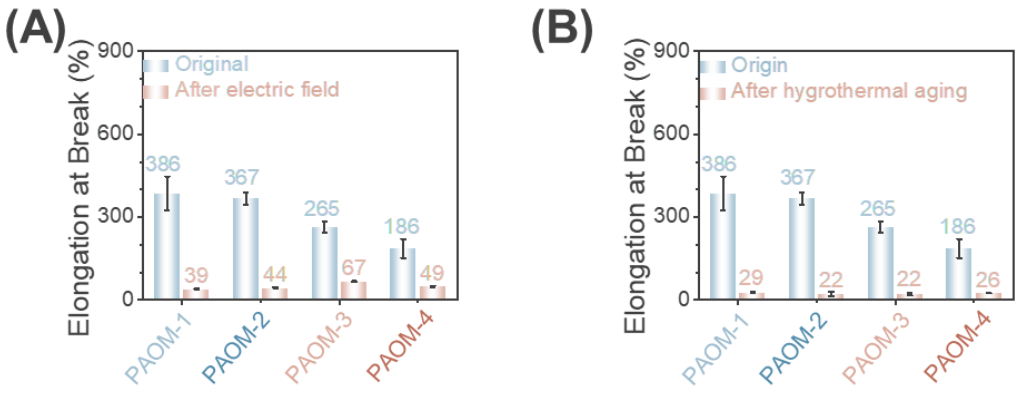

346

347 **Figure S15.** (A, B) Elongation break after electric field and hygrothermal aging of

348 PAOM.

349

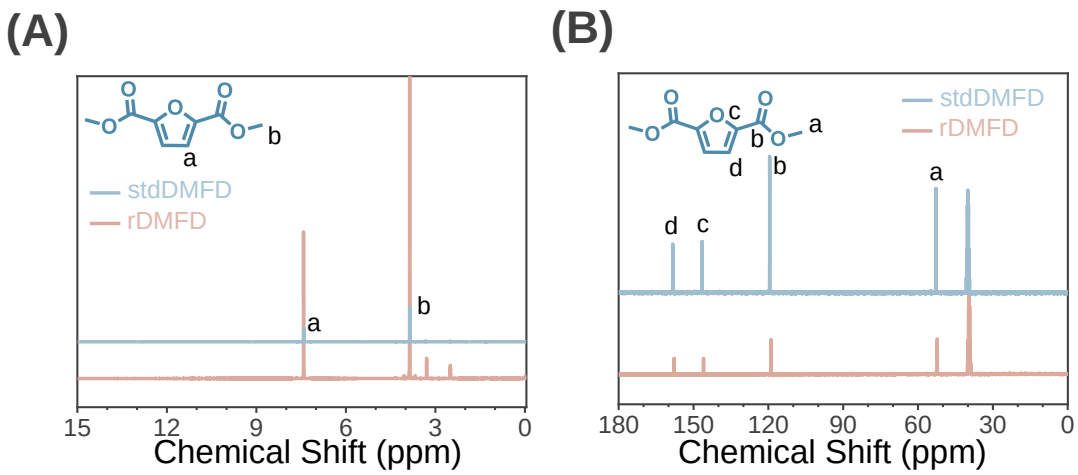

350

351 **Figure S16.** (A)^{1}H NMR spectra of standard DMFD (stdDMFD) and rDMFD obtained

352 from PAOM recycling experiment, (B) ^{13}C NMR spectra of standard DMFD (std

353 DMFD) and rDMFD obtained from PAOM recycling experiment.

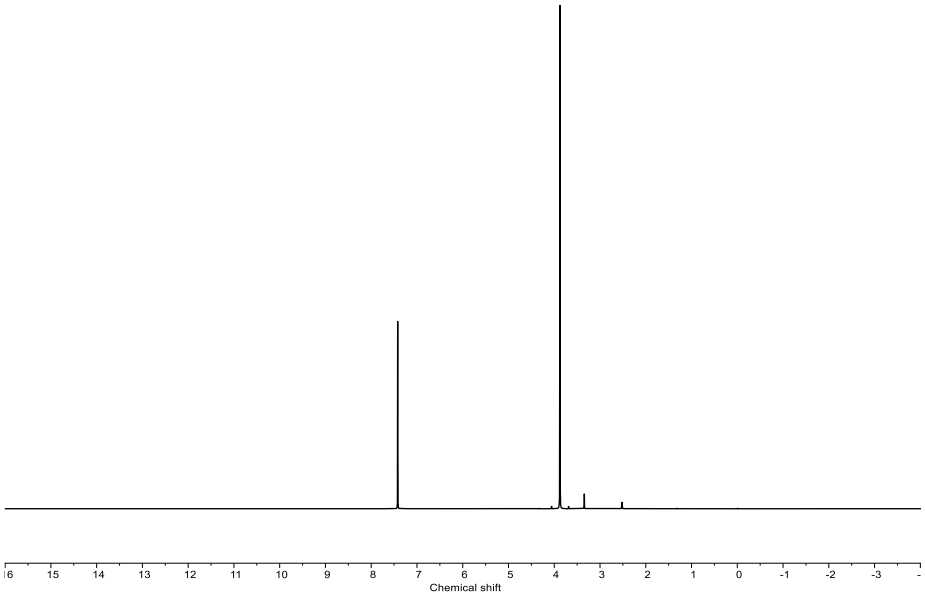

354

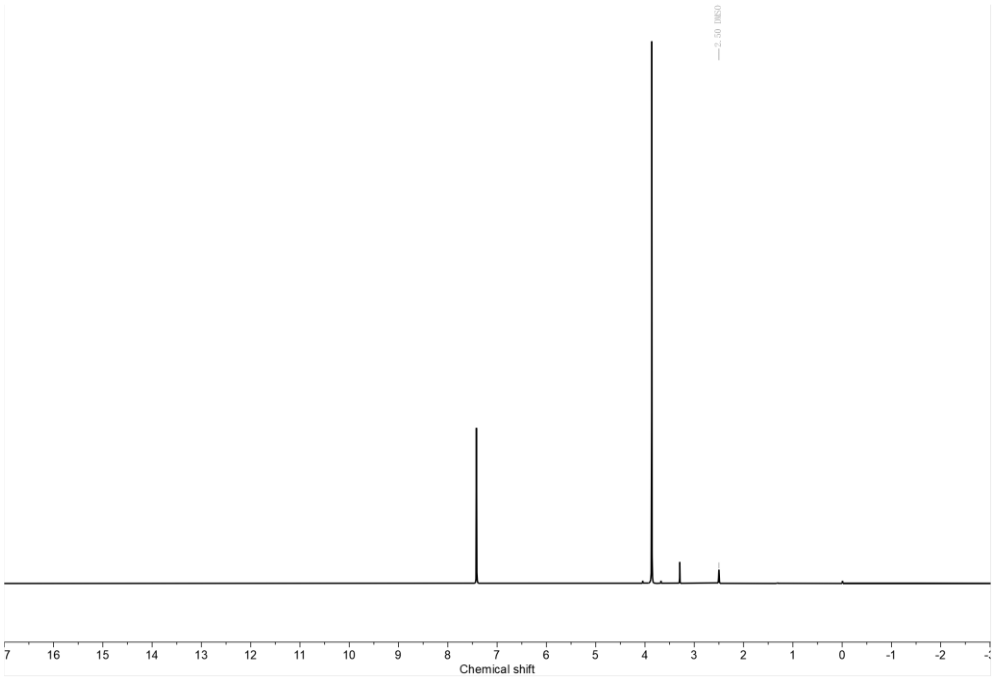

355

356 **Figure S17.** ^{1}H NMR spectra of DMFD (stdDMFD) and rDMFD.

357

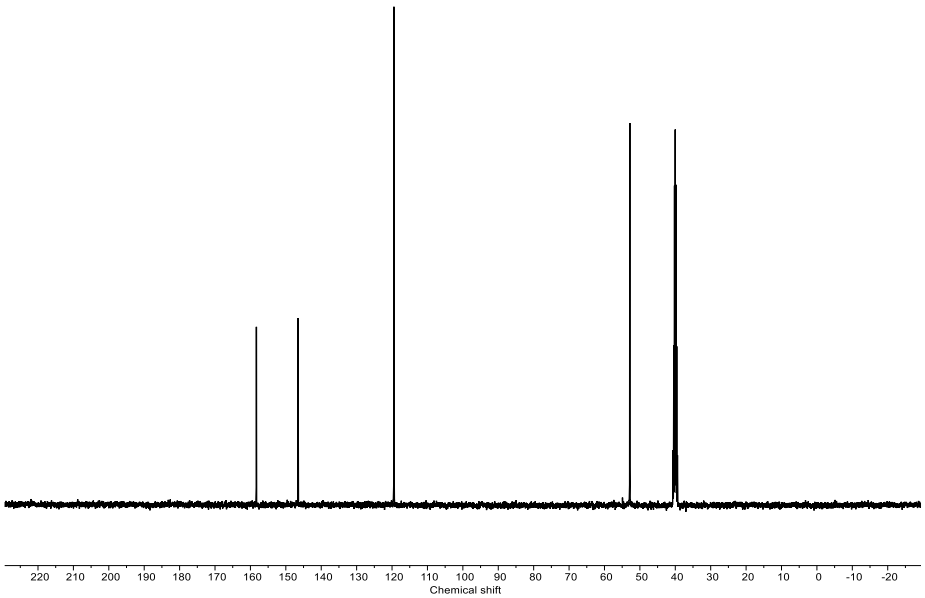

358

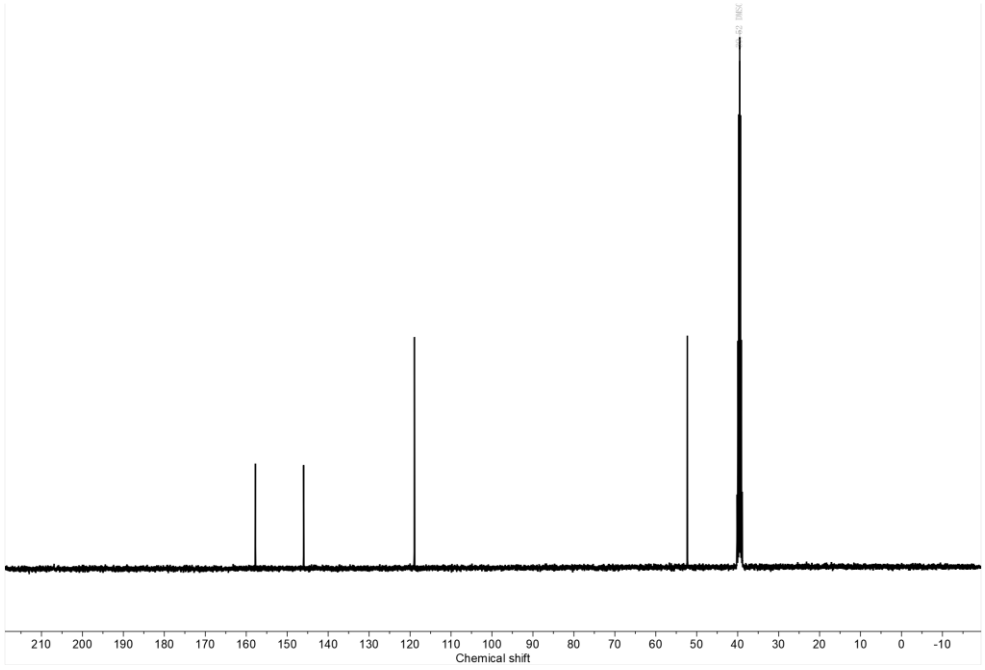

359

360 **Figure S18.** ^{13}C NMR DMFD (stdDMFD) and rDMFD.

361

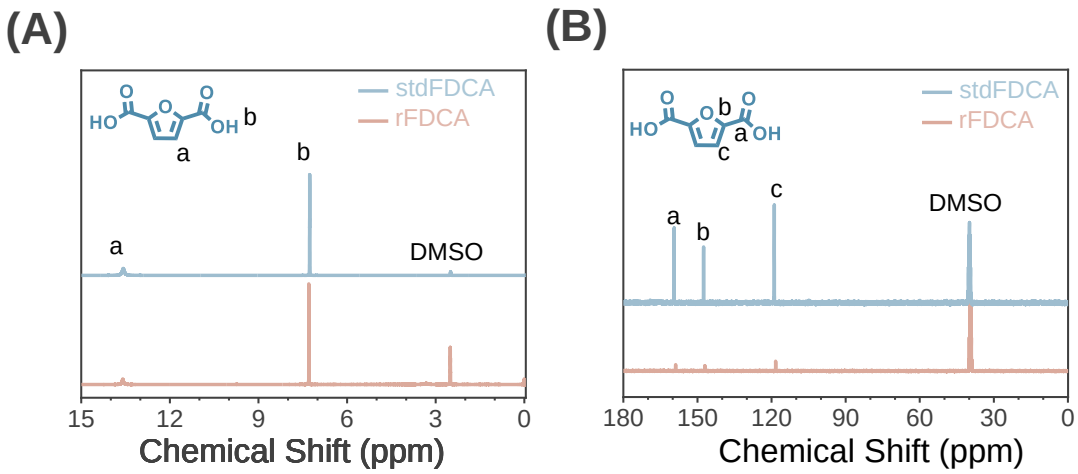

Figure S19. (A)^{1}H NMR spectra of standard FDCA (stdFDCA) and rFDCA obtained from PAOM recycling experiment, (B) ^{13}C NMR spectra of standard FDCA (stdFDCA)

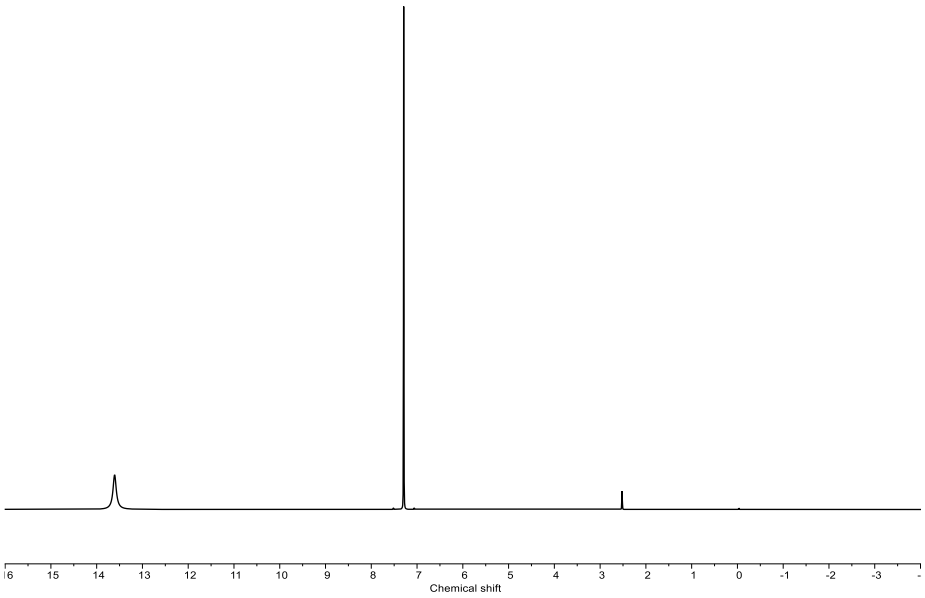

366

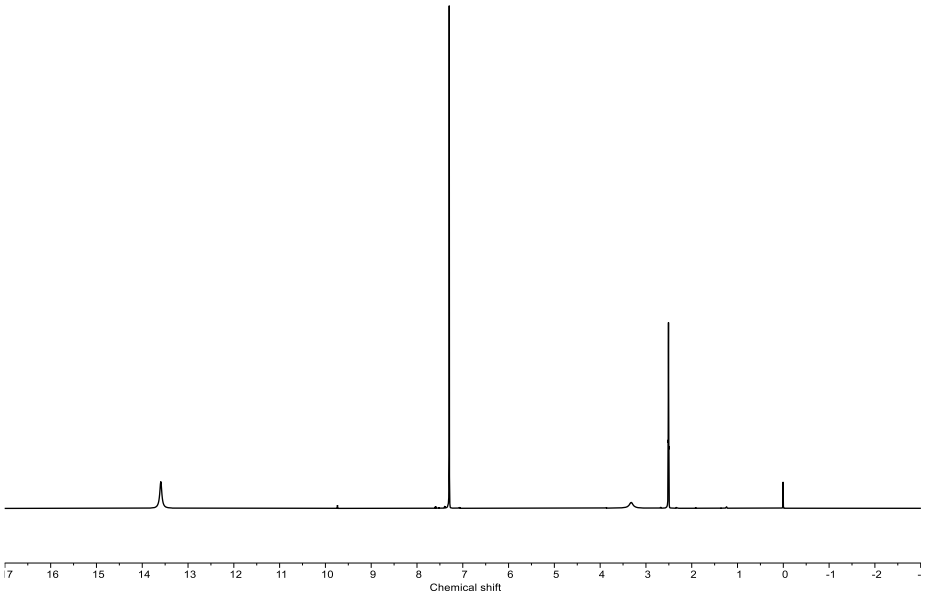

367

368 **Figure S20.** ^{1}H NMR spectra of FDCA (stdFDCA) and rFDCA.

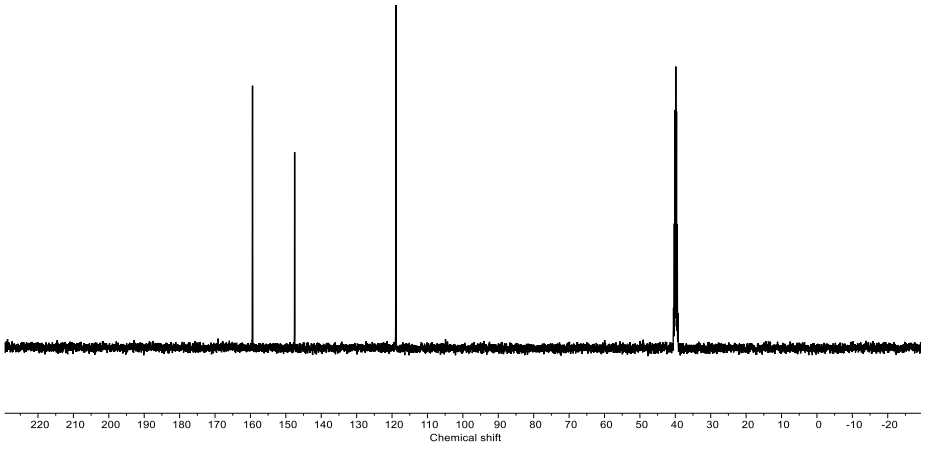

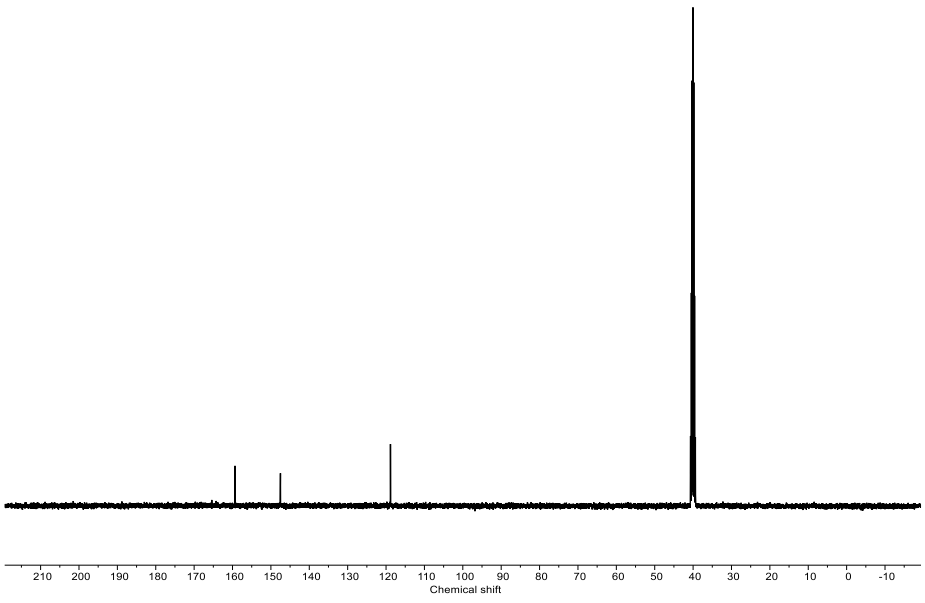

Figure S21. ^{13}C NMR spectra of FDCA (stdFDCA) and rFDCA.

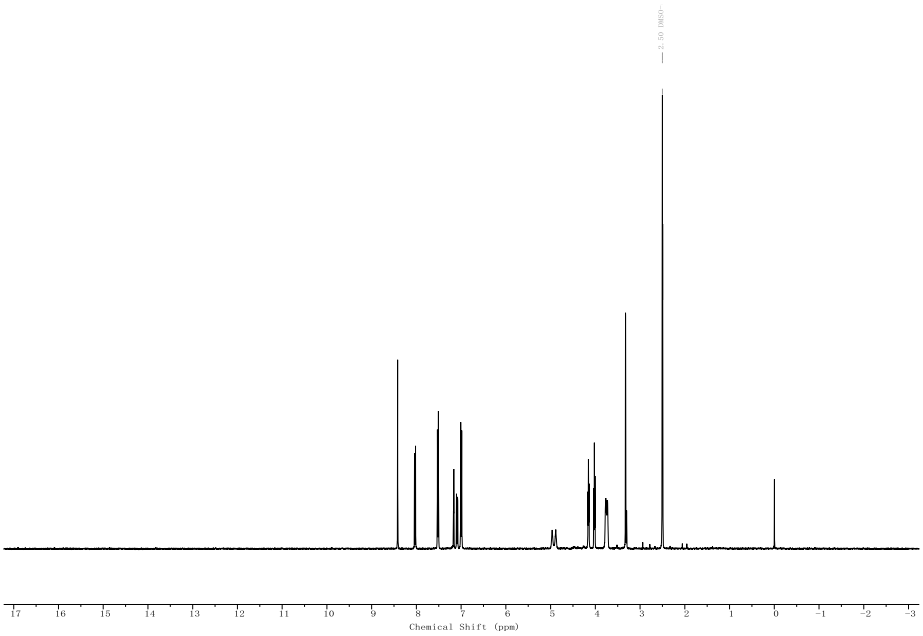

373

374 **Figure S22.** ^{1}H NMR spectra of DDF-OH.

375

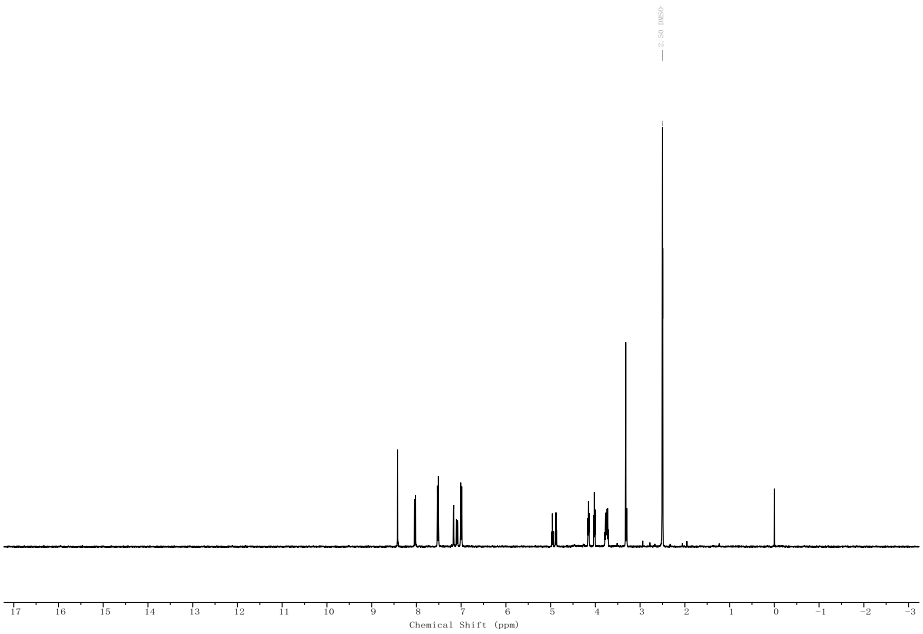

376

377 **Figure S23.** ^{1}H NMR spectra of rDDF-OH.

378

379

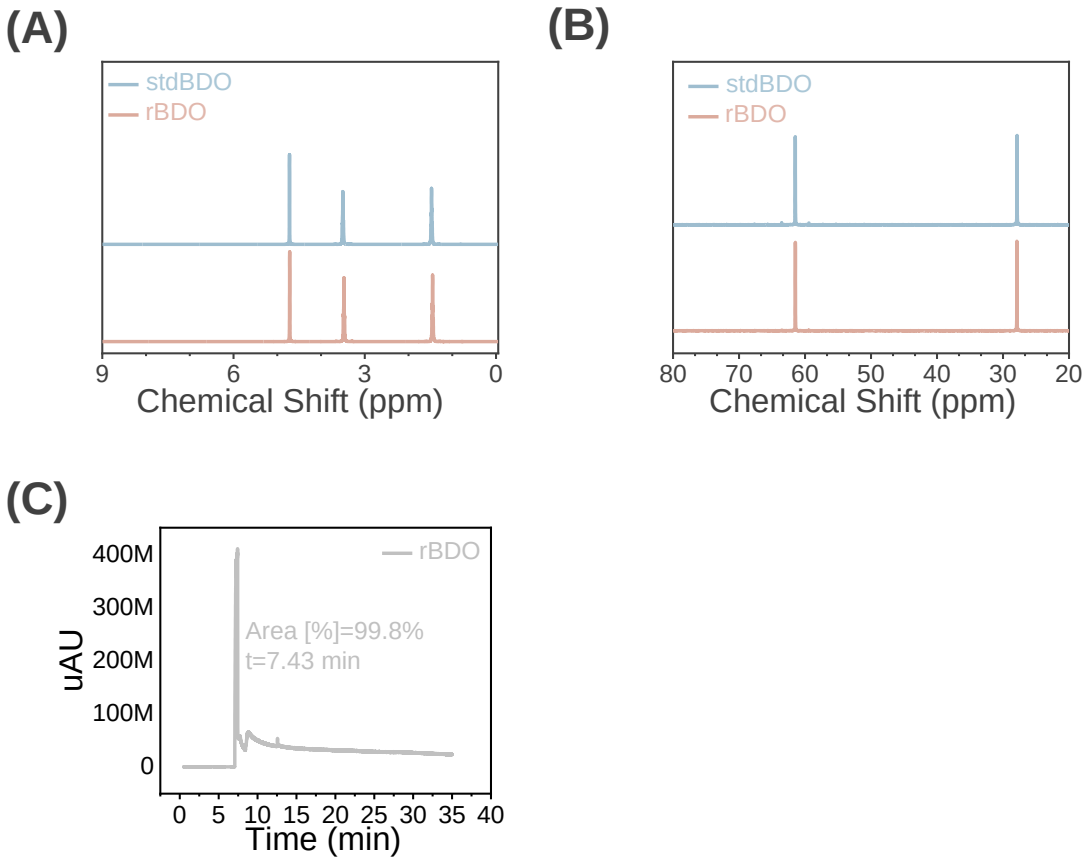

380

381 **Figure S24.** (A) ^{1}H NMR spectra of standard BDO (stdBDO) and rBDO obtained from

382 PAOM recycling experiment, (B) ^{13}C NMR spectra of standard BDO (stdBDO) and

383 rBDO obtained from PAOM recycling experiment, (C) LC trace of rBDO obtained from

384 recycling experiment.

385

386

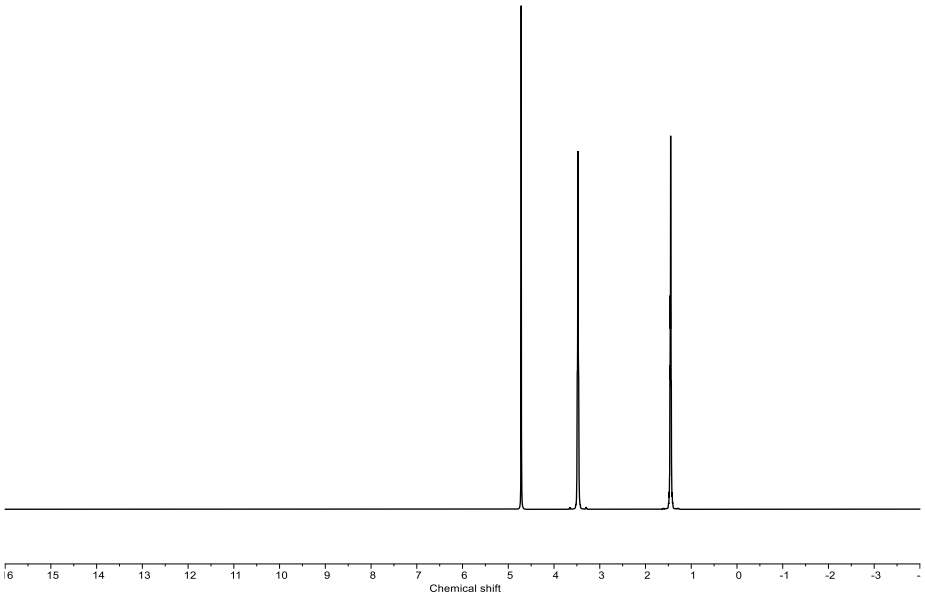

387

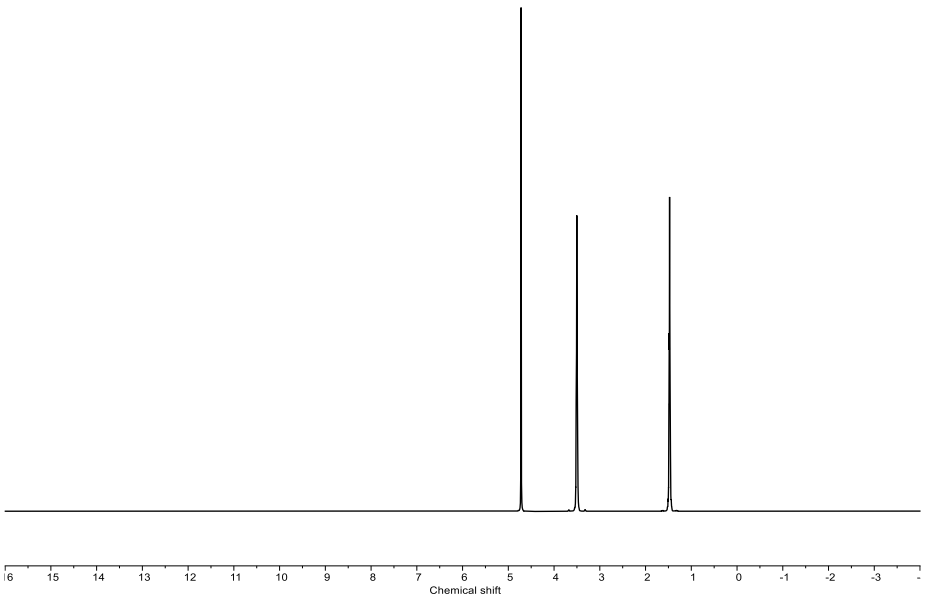

388 **Figure S25.** ^{1}H NMR spectra of BDO (stdBDO) and rBDO.

389

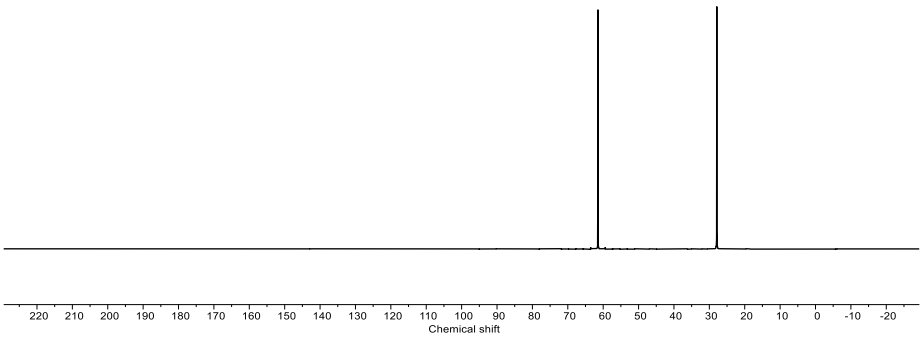

390

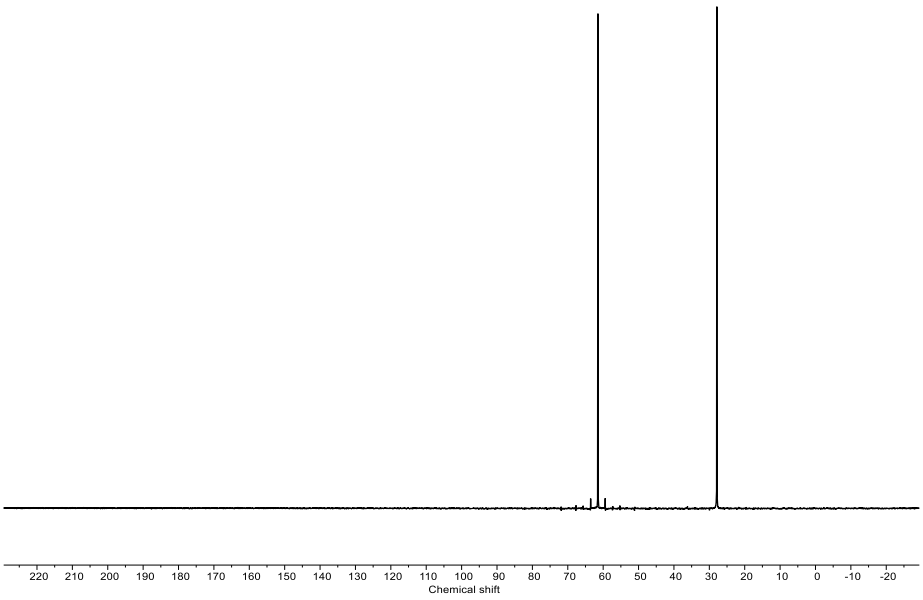

391

392 **Figure S26.** ^{13}C NMR spectra of BDO (stdBDO) and rBDO.

393

394

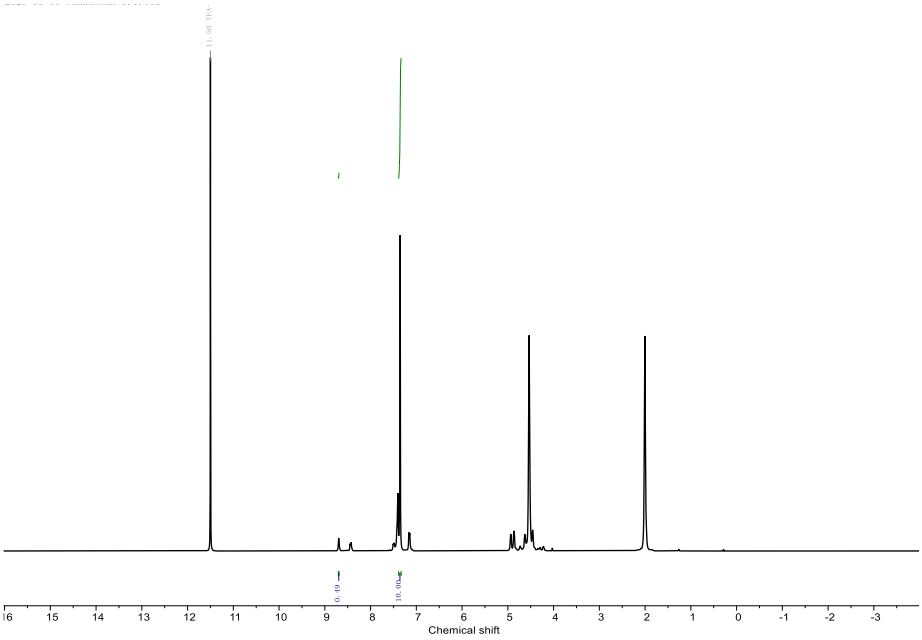

Figure S27. ^{1}H NMR spectra of PAOM-4.

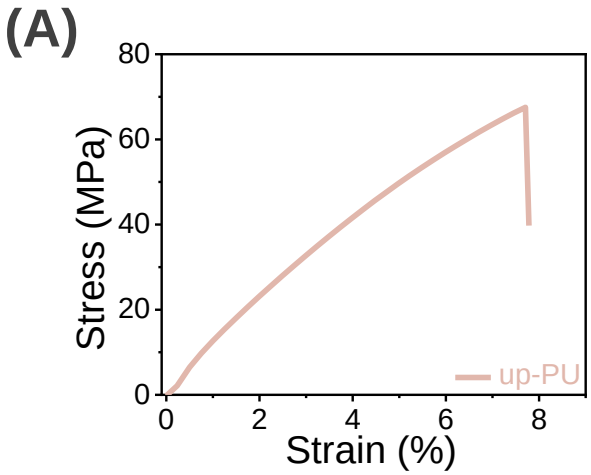

Figure S28. Stress-strain curve of up-Pu.

References

[1] Lu, T., Chen, F. Multiwfn: A multifunctional wavefunction analyzer. *Journal of computational chemistry* 2012, *33*, 580-592. https://onlinelibrary.wiley.com/doi/10.1002/jcc.22885

[2] Zhang, J., Lu, T. Efficient evaluation of electrostatic potential with computerized optimized code. *Phys Chem Chem Phys* 2021, *23*, 20323-20328. https://pubs.rsc.org/en/content/articlelanding/2021/CP/D1CP02099K

[3] Martínez, L., Andrade, R., Birgin, E. G., Martínez, J. M. PACKMOL: A package for building initial configurations for molecular dynamics simulations. *Journal of computational chemistry* 2009, *30*, 2157-2164. https://onlinelibrary.wiley.com/doi/10.1002/jcc.21224

[4] Abraham, M. J., Murtola, T., Schulz, R., Páll, S., Smith, J. C., Hess, B., Lindahl, E. GROMACS: High performance molecular simulations through multi-level parallelism from laptops to supercomputers. *SoftwareX* 2015, *1*, 19-25. https://www.sciencedirect.com/science/article/pii/S2352711015000059

[5] Sambasivarao, S. V., Acevedo, O. Development of OPLS-AA force field parameters for 68 unique ionic liquids. *Journal of chemical theory and computation* 2009, *5*, 1038-1050. https://pubs.acs.org/doi/10.1021/ct800578q

[6] Humphrey, W., Dalke, A., Schulten, K. VMD: visual molecular dynamics. *Journal of molecular graphics* 1996, *14*, 33-38. https://www.sciencedirect.com/science/article/pii/0263785596000185

[7] Dlubek, G., Saarinen, K. & Fretwell, H. The temperature dependence of the local free volume in polyethylene and polytetrafluoroethylene: a positron lifetime study. *Journal of Polymer Science Part B: Polymer Physics* **36**, 1513-1528 (1998). https://onlinelibrary.wiley.com/doi/10.1002/(SICI)1099-0488(19980715)36:9<1513::AID-POLB10>3.0.CO;2-7

[8]Shantarovich, V., Kevdina, I., Yampolskii, Y. P. & Alentiev, A. Y. Positron annihilation lifetime study of high and low free volume glassy polymers: effects of free volume sizes on the permeability and permselectivity. *Macromolecules* **33**, 7453-7466 (2000). https://pubs.acs.org/doi/10.1021/ma0001251

[9]Hougham, G. G. & Jean, Y. C. Relative Contributions of Polarizability and Free Volume in Reduction of Refractive Index and Dielectric Constant with Fluorine Substitution in Polyimides by Positron Annihilation Spectroscopy. *Macromolecular Chemistry and Physics* **215**, 103-110 (2014). https://doi.org/10.1002/macp.201300430

[10] Ishida, T., Kitagaki, R., Hagihara, H. & Elakneswaran, Y. Role of Moisture in Photo-ageing -macromolecular Architecture Evolution of Acrylic-urethane Network. *Polymer Testing* **96**, 107123 (2021). https://doi.org/10.1016/j.polymertesting.2021.107123

[11] Mane, P., Keche, A. J., Chopra, S. & Pande, K. Effect of Polycarbonate (PC) Content on the Mechanical Properties, Morphology and Transesterification Mechanism of PBT/PC Immiscible Blends. *Journal of Applied Polymer Science* **141**, e55902 (2024). https://doi.org/10.1002/app.55902

[12] Wu, Y. *et al.* Multiple-functional Molecularly Imprinted Nanocomposite Membranes for High-efficiency Selective Separation Spplications: An Imitated Core-shell TiO2@PDA-based MIMs Design. *Composites Part B: Engineering* **198**, 108123 (2020). https://doi.org/10.1016/j.compositesb.2020.108123

[13] Liang, Y. *et al.* Municipal Sewage Sludge Incineration and its Air Pollution Control. *Journal of Cleaner Production* **295**, 126456 (2021). https://doi.org/10.1016/j.jclepro.2021.126456

[14] Sit, S., Chakraborty, G. & Das, N. C. Superior EMI Shielding Effectiveness with Enhanced Electrical Conductivity at Low Percolation Threshold of Flexible Novel Ethylene Methyl Acrylate/single-walled Carbon Nanotube Nanocomposites. *Polymer Engineering & Science* **62**, 2047-2060 (2022). https://doi.org/10.1002/pen.25987

[15] Nikbakht Nasrabadi, M., Sedaghat Doost, A. & Mezzenga, R. Modification Approaches of Plant-based Proteins to Improve Their Techno-functionality and Use in Food Products. *Food Hydrocolloids* **118**, 106789 (2021). https://doi.org/10.1016/j.foodhyd.2021.106789

[16] Wang, W. *et al.* Bubble-based Microrobot: Recent Progress and Future Perspective. *Sensors and Actuators A: Physical* **360**, 114567 (2023). https://doi.org/10.1016/j.sna.2023.114567

[17] Wang, S. *et al.* Theoretical Modeling and Experimental Verification of Percolation Threshold with MWCNTs' Rotation and Translation Around a Growing Bubble

in Conductive Polymer Composite Foams. *Composites Science and Technology* **199**, 108345 (2020). https://doi.org/10.1016/j.compscitech.2020.108345

[18] Garrell, M. G., Ma, B.-M., Shih, A. J., Lara-Curzio, E. & Scattergood, R. O. Mechanical Properties of Polyphenylene-sulfide (PPS) Bonded Nd–Fe–B Permanent Magnets. *Materials Science and Engineering: A* **359**, 375-383 (2003). https://doi.org/10.1016/s0921-5093(03)00400-3

[19] Xie, K., Li, Z., Zhao, B., Guo, Z. & Deng, X. Construction of Fluorenyl-modified Low Dielectric Constant Polyimide Films with Excellent Mechanical Properties and Optical Transparency. *Journal of Applied Polymer Science* **141**, e55217 (2024). https://doi.org/10.1002/app.55217

[20] Quinn, E. C. *et al.* Installing Controlled Stereo-Defects Yields Semicrystalline and Biodegradable Poly(3-Hydroxybutyrate) with High Toughness and Optical Clarity. *Journal of the American Chemical Society* **141**, 5795–5802 (2023). https://doi.org/10.1021/jacs.2c12897

[21] Zhao, T.-H., Yuan, W.-Q., Li, Y.-D., Weng, Y.-X. & Zeng, J.-B. Relating Chemical Structure to Toughness via Morphology Control in Fully Sustainable Sebacic Acid Cured Epoxidized Soybean Oil Toughened Polylactide Blends. *Macromolecules* **51**, 2027–2037 (2018). https://doi.org/10.1021/acs.macromol.8b00103

[22] Li, X. L. *et al.* A Multifunctional Bio-Based Polyester Material Integrated with High Mechanical Performance, Gas Barrier Performance, and Chemically Closed-

Loop. *Advanced Functional Materials* **34**, 2400911 (2024). https://doi.org/10.1002/adfm.202400911

[23] Zhou, L. *et al.* Chemically Circular, Mechanically Tough, and Melt-processable Polyhydroxyalkanoates. *Science* **380**, 64-69 (2023).

[24] Jagannath, J., Nadanasabapathi, S. & Bawa, A. Effect of Starch on Thermal, Mechanical, and Barrier Properties of Low Density Polyethylene Film. *Journal of applied polymer science* **99**, 3355-3364 (2006).

[25] Jacquelot, E., Espuche, E., Gérard, J. F., Duchet, J. & Mazabraud, P. Morphology and Gas Barrier Properties of Polyethylene-based Nanocomposites. *Journal of Polymer Science Part B: Polymer Physics* **44**, 431-440 (2006).

[26] Marangoni Junior, L. *et al.* High-pressure Processing Effects on the Barrier Properties of Flexible Packaging Materials. *Journal of Food Processing and Preservation* **44**, e14865 (2020).

[27] Yi, J. *et al.* Development of a Series of Biobased Poly(ethylene 2,5-furandicarboxylate-co-(5,5′-((phenethylazanediyl)bis(methylene))bis(furan-5,2-diyl))dimethylene 2,5-furandicarboxylate) Copolymers via a Sustainable and Mild Route: Promising "Breathing" Food Packaging Materials. *Green Chemistry* **24**, 5181-5190 (2022). https://doi.org/10.1039/d2gc01214f

[28]Nuruddin, M. *et al.* Gas and Water Vapor Barrier Performance of Cellulose Nanocrystal–Citric Acid-Coated Polypropylene for Flexible Packaging. *ACS Applied Polymer Materials* **2**, 4405-4414 (2020). https://doi.org/10.1021/acsapm.0c00483